

Research



Cite this article: Lin H, Lu C, Wang HY, Dai

LH. 2020 Non-trivial avalanches triggered by shear banding in compression of metallic glass foams. *Proc. R. Soc. A* **476**: 20200186.

<http://dx.doi.org/10.1098/rspa.2020.0186>

Received: 18 March 2020

Accepted: 17 July 2020

Subject Areas:

geophysics, complexity, materials science

Keywords:

metallic glass foam, shear banding, avalanches

Authors for correspondence:

L. H. Dai

e-mail: lhdai@lnm.imech.ac.cn

H. Lin

e-mail: linhao@imech.ac.cn

Electronic supplementary material is available online at <https://doi.org/10.6084/m9.figshare.c.5077979>.

Non-trivial avalanches triggered by shear banding in compression of metallic glass foams

H. Lin^{1,2}, C. Lu³, H. Y. Wang^{1,2} and L. H. Dai^{1,2}

¹State Key Laboratory of Nonlinear Mechanics, Institute of Mechanics, Chinese Academy of Sciences, Beijing 100190, People's Republic of China

²School of Engineering Science, University of Chinese Academy of Sciences, Beijing 101408, People's Republic of China

³School of Civil and Mechanical Engineering, Curtin University, Western Australia 6845, Australia

CL, 0000-0002-7368-8104; LHD, 0000-0001-8991-0358

Ductile metallic glass foams (DMGFs) are a new type of structural material with a perfect combination of high strength and toughness. Owing to their disordered atomic-scale microstructures and randomly distributed macroscopic voids, the compressive deformation of DMGFs proceeds through multiple nanoscale shear bands accompanied by local fracture of cellular structures, which induces avalanche-like intermittences in stress–strain curves. In this paper, we present a statistical analysis, including distributions of avalanche size, energy dissipation, waiting times and aftershock sequence, on such a complex dynamic process, which is dominated by shear banding. After eliminating the influence of structural disorder, we demonstrate that, in contrast to the mean-field results of their brittle counterparts, scaling laws in DMGFs are characterized by different exponents. It is shown that the occurrence of non-trivial scaling behaviours is attributed to the localized plastic yielding, which effectively prevents the system from building up a long-range correlation. This accounts for the high structural stability and energy absorption performance of DMGFs. Furthermore, our results suggest that such shear banding dynamics introduce an additional characteristic time scale, which leads to a universal gamma distribution of waiting times.

1. Introduction

Fracture of inhomogeneous materials is common in nature. Different from the catastrophic failure of brittle materials, microcracks in a disordered medium proceed with intermittent avalanches, which can be characterized by power laws [1–10]. These scale-free behaviours are usually considered to be signatures of collective phenomena and of importance in predicting material failure. Recently, similar scaling laws have been found in the compression of small and brittle porous materials [11–14], which may provide a correlation between avalanches that extend from geophysical scales (of the order of hundreds of kilometres) to sample scales (of the order of a few millimetres). The mean-field theory [15–18], neglecting the relevance of detailed physics, has been successfully applied to the explanation of these phenomena, together with universal scaling laws and exponents corresponding to experimental observations in brittle fracture [11–18].

Compared with simple brittle fracture, shear banding, which is a more general form of damage fracture that is widely observed in natural fault zones [19–25] and plastic deformation of metallic glasses [26–29], is more complicated. Highly localized deformation induces plastic instability, which is also manifested as stick-slip sliding. In these cases, a large amount of energy is dissipated in a narrow region, which results in a significant temperature rise and rheological change of local materials, i.e. the viscoelastic effect. Such additional physical processes usually introduce different characteristic time scales and act as effective dissipation sources preventing critical failure [30,31]. This may lead to scaling behaviours much closer to seismicity than brittle fracture of heterogeneous materials; these behaviours have been discussed by using various seismic models with microscopic mechanisms such as rheology damage [32,33], rate-and-state-dependent friction [34] and viscoelasticity [35–37]. However, direct experiments comparing scaling behaviours of fracture and avalanches triggered by localized plastic events are still lacking, which results in the critical issue under debate: these two processes, dominated by fracture and shear banding, are either statistically indistinguishable, such that they can be described under a unified model, or distinguishable, such that traces reflecting their micro-dynamics can be captured from the analysis of mechanical noise.

Ductile metallic glass foams (DMGFs) are a new type of structural material with cross-scale disorders, i.e. disordered atomic-scale microstructures and randomly distributed millimetre voids. Unlike crystalline metals and alloys, metallic glasses do not exhibit long-range translational symmetry. Thus, plastic deformation in metallic glasses is usually through shear transformation zones, which are attributed to collective rearrangements of 10–100 atoms [26–29]. At room temperature and high stress, the deformation of metallic glasses is localized into shear bands, which is what also happens in natural fault zones [19–22]. On the other hand, owing to the existence of macroscopic voids in DMGFs, catastrophic failures dominated by a single crack can be effectively prevented. Thus, the deformation of DMGFs proceeds through multiple nanoscale shear bands prior to local fracture of cellular structures, which induces avalanche-like intermittences in stress–strain curves [38,39].

In this paper, we present the detailed statistics of such a dynamic process in the compression of DMGFs, where localized plastic deformation is the dominant dissipation pattern, and compare them with fracture avalanches in a typical brittle porous material. In contrast to a brittle material, the deformation of DMGFs exhibits fundamental scaling laws with exponents beyond the estimation of the mean-field theory, suggesting a different universality class. This can be attributed to additional plasticity, which prevents the system from building up long-range correlations and accounts for the high structural stability and energy absorption performance of DMGFs. Furthermore, we show that, by introducing a characteristic time scale, such shear banding plasticity leads to a universal gamma distribution of waiting times, and faster Omori decaying triggered events. Considering the existence of an internal characteristic time, we derive a general scaling relation among these scaling exponents, which is in good accordance with our experiments.

2. Experiments and definitions of avalanches

Cylindrical DMGFs with diameter 10 mm and porosity $\phi = 60\%$ were fabricated by pressure infiltration combined with rapid cooling, as shown in appendix Aa. For comparison, brittle alumina foams (BAFs) with diameter 30 mm and porosity $\phi = 80\%$ were also prepared. Experiments on brittle porous materials with different porosities have been reported, and there was no observed deviation [12]. This is because, after a long loading process, the continuous accumulation of cracks, replacing the initial porosity, becomes a main part of the system's heterogeneity. It is clearly different from a short-term loading process, where the initial geometry controls the system's heterogeneity [40]. The fundamental mechanical properties of metallic glasses $\text{Zr}_{41.25}\text{Ti}_{13.75}\text{Cu}_{12.5}\text{Ni}_{10}\text{Be}_{22.5}$ (Vit 1) and Al_2O_3 are listed in table 1. Uniaxial compression tests were carried out on an MTS-810 material test system at room temperature.

Within the context of structural phase transitions, avalanche scale invariance can be manifested in different ways depending on the driving mechanisms [41]. If the control variable is force, disorder leads to a dominant nucleation process. The criticality can be reached by tuning the external driving force. However, if the driving force is a constant velocity, the system will spontaneously evolve into a stationary critical point at which the velocity vanishes, i.e. the self-organized criticality. The influence of a driving mechanism on slip avalanches was studied in compressed microcrystals [42]. Here, we focus on the displacement-driven mode with a slow strain rate of 10^{-3} s^{-1} for all samples, which can be considered as the most common loading form in nature [43].

The force on a sample was measured with a resolution of 0.1 N, and the sampling frequency was set as 100 Hz, which has enough precision to record each peak or critical stress. The total accumulated experimental duration is 800 s. Instead of smooth deformation, jerky flow was observed in these two porous materials; however, their underlying physical processes are essentially different. As illustrated in figure 1a, deformation of BAFs proceeds by brittle fracture of disordered cellular structures along a main crack or several sub-crack tips, leading to the first major drop in the force– or stress–time curves; in DMGFs, plastic strain is locally accumulated in the cellular walls by formation of multiple nanoscale shear bands before final fracture, and such an additional process can effectively avoid a larger rift valley throughout the entire structure and the occurrence of extreme stress drops, resulting in a stable stress platform [38,39]. The typical force–time curves for BAFs and DMGFs are shown in figure 1b,c, respectively. Before the final compaction, there are hundreds of sudden stress drops accompanied by acoustic emission (AE) signals.

As is well known, avalanches in brittle materials are usually quantified by the AE energy [44,45], where the captured signals are elastic vibrations caused by fracture or friction rebound. However, taking cellular structures into account, a part of the energy is lost through the dispersion of stress waves near the surfaces of cavities. On the other hand, because of the high toughness of DMGFs (table 1), a large proportion of energy is used to form new fracture surfaces and is dissipated in nanoscale shear bands. It is difficult to accurately estimate this part of the released energy by using AE signals. To overcome this obstacle, we resort to fluctuating force signals as provided in the electronic supplementary material to directly measure avalanche sizes [46–48] and their corresponding released energy.

Here, two definitions of avalanche size are adopted to characterize the dynamic process of deformation. The first one is the commonly used instant stress drop or strain burst, which reflects the transient instability. Compared with the direct measurement of the stress drop, we can obtain a higher spatial resolution by calculating the irreversible displacement increment, Δx_j , as shown in appendix Ab. Let us consider the signal of external force, $F(t)$, as illustrated in figure 1d. The local burst displacement is calculated by

$$\Delta x_j = \frac{F_{\max,j}}{k_{j-1}} - \frac{F_{\min,j}}{k_j}, \quad (2.1)$$

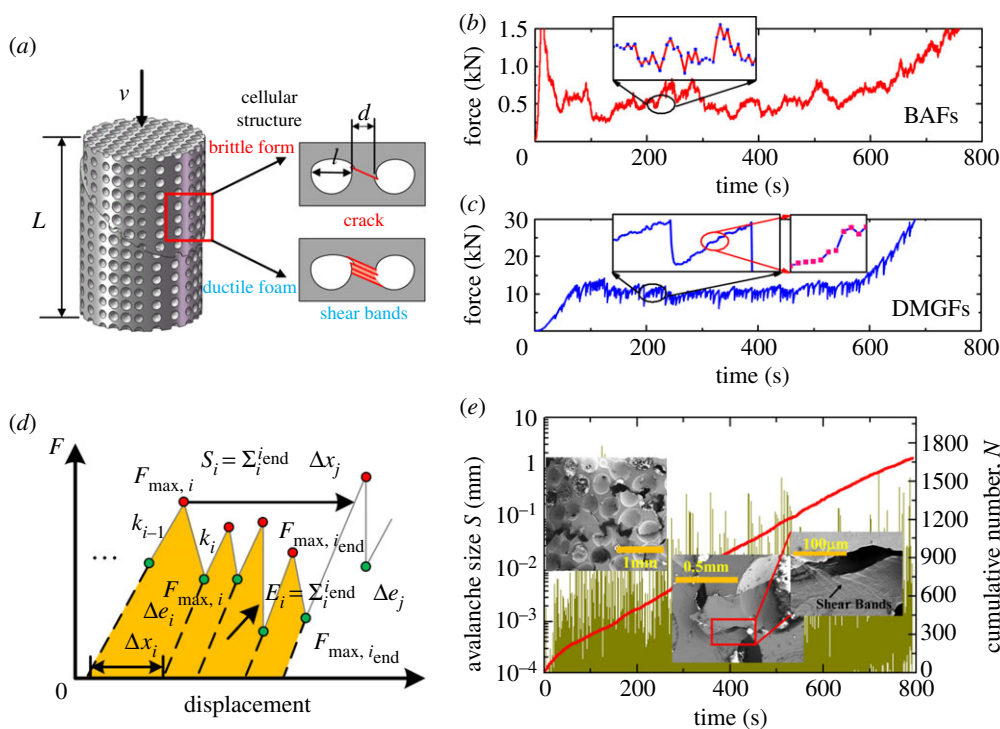


Figure 1. (a) Illustration of microscopic deformation in the two types of porous materials. (b,c) Typical force–time curves (with a constant strain rate of $1 \times 10^{-3} \text{ s}^{-1}$) for BAFs and DMGFs, respectively, with (d) the definitions of avalanche size, S , and energy dissipation, E . (e) The time evolution of avalanche size defined by equation (2.2), and the total number of events in DMGFs, where insets are microscopic damage images of a full view, collapsed cellular structures and a local zoom of a fractured skeleton (from left to right) during compression. (Online version in colour.)

Table 1. Mechanical properties of matrix materials (Vit 1 and Al_2O_3), including Young's modulus E , yield or breaking strength $\sigma_{s,b}$, fracture strain ϵ_f under uniaxial compression and fracture toughness K_{Ic} .

matrix	E (GPa)	$\sigma_{s,b}$ (GPa)	ϵ_f (%)	K_{Ic} ($\text{MPa} \cdot \text{m}^{-1/2}$)
Vit 1	97	1.8	2.3	52
Al_2O_3	370	3	0.8	3 ~ 4

where $F_{\max,j}$ (or $F_{\min,j}$) and k_j are the local maximum (or minimum) force and stiffness at time t_j during the time interval $[t_i, t_{i_{\text{end}}}]$, respectively.

The second one defines bursts as ‘valleys’ in a force–displacement curve [46]. Based on this definition, an avalanche corresponding to time t_i is the total of the irreversible deformation increments in the forward direction (figure 1d), that is,

$$S_i = \sum_{j=i}^{i_{\text{end}}} \Delta x_j, \quad (2.2)$$

in an interval starting from a current yield stress, $F_{\max,i}$, to a larger one, $F_{\max,i_{\text{end}}+1}$. Different from the former, the latter concatenates smaller transient burst events, and thus can reflect the non-instantaneous and non-local stability.

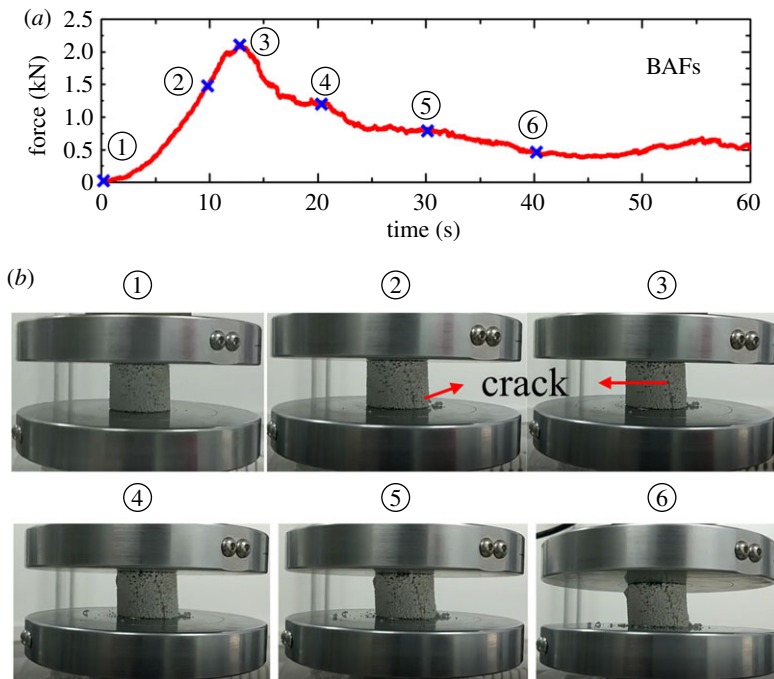


Figure 2. Zoom of a force–time curve for BAFs at the initial deformation stage (*a*) and several typical macrofracture morphologies chosen from it (*b*), which cover the main characteristics of deformation and failure before and after the first major stress drop. (Online version in colour.)

In addition, we can also define the energy dissipation during each avalanche Δe_i corresponding to the first definition and E_i to the second one, where

$$E_i = \sum_{j=i}^{i_{\text{end}}} \Delta e_j. \quad (2.3)$$

Obviously, Δe_j and E_i are equal to the area of a force–displacement curve under the respective definitions of avalanche size (figure 1*d*), which are related to the seismic moment of earthquakes [49]. With the time evolution, we can obtain earthquake-like avalanche series. Each sample produces typically a few thousand events (1700 ± 500) for DMGFs, and tens of thousands of events ($16\,000 \pm 1000$) for BAFs. Figure 1*e* shows the typical time evolution of avalanche events (with size more than 100 nm) and their cumulative numbers (counted at intervals of 0.1 s) for DMGFs. Owing to the distributed nanoscale shear bands, severe plastic energy dissipation is extremely limited in a narrow region accompanied by strain or thermal softening [50] before local fracture of skeletons. Figure 2 shows the zoom of a force–time curve for BAFs at the initial deformation stage and several typical macrofracture morphologies chosen from it, which cover the main characteristics of deformation and failure before and after the first major stress drop. A main crack splitting longitudinally across the whole sample, which is typical of brittle failure, leads to a precipitous drop in its carrying capacity.

No matter whether they are on the macroscopic or microscopic scale, the deformation and failure mechanisms for DMGFs are very different from those for BAFs. Figure 3 exhibits scanning electron microscope (SEM) images of DMGFs at different strain stages. The observation was first conducted at a strain of approximately 2.5%, where the specimen just suffered a stress drop (figure 3*a*). It can be seen that many local and nonfatal shear fractures, as indicated by the arrows, occurred in struts. Unlike catastrophic brittle fracture in BAFs, plastic shear bands in

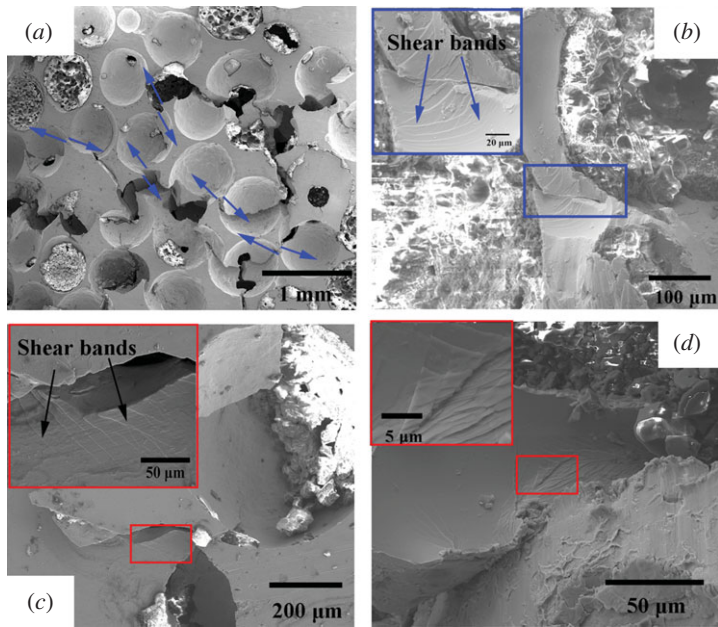


Figure 3. SEM images of DMGFs at different strain stages. (a) $\epsilon \approx 2.5\%$, (b) $\epsilon \approx 3\%$, (c) $\epsilon \approx 5\%$ and (d) $\epsilon \approx 75\%$. (Online version in colour.)

DMGFs correspond to local unstable slips that can be stopped by cavitations, leading to a non-zero sticking stress, as shown in figure 3*b*. As loading continues, crushed struts come into contact with each other (figure 3*c*), which leads to elastic reloading until stress exceeds the strength. Then, a subsequent stress drop occurs and the stress redistributes in the whole sample. However, the loading state becomes much more complicated than the initial one. The inset in figure 3*c* presents the detail of a broken strut: multiple shear bands formed under a bending load that ensures a relatively stable deformation. Figure 3*d* shows interruption at a strain of approximately 75%, which is close to the densification strain (see inset for details). The high density of shear bands indicates that the matrix has also accommodated a considerable deformation besides the collapse of the struts.

3. Results and discussion

(a) Avalanche statistics based on the first definition

To obtain the maximum resolution of a limited experimental dataset, the complementary cumulative distribution function (CCDF) is used. As shown in figure 4*a,c*, the CCDF of avalanche size exhibits a power-law characteristic, i.e. $\text{CCDF}(\Delta x) \sim \Delta x^{-(\tau_{\Delta x}-1)}$, over several magnitudes for both BAFs and DMGFs, suggesting scale-free and self-similarity in their fracture and localized plastic dynamics. The corresponding probability density functions are $P(\Delta x) \sim \Delta x^{-\tau_{\Delta x}}$, with $\tau_{\Delta x} = 2.0 \pm 0.1$ for BAFs and $\tau_{\Delta x} = 1.90 \pm 0.07$ for DMGFs, implying a material-independent exponent, $\tau_{\Delta x} = 2$. The same exponent, $\tau_{\Delta e} = 2$, was also found in energy dissipation distributions (figure 4*b,d*), with a linear relationship between Δx and Δe .

Here, it is worth noting that, once the spatial distribution of avalanches becomes larger than 2, the mean avalanche size becomes finite and is independent of the system size. This is significantly different from the mean-field criticality, where $\tau = 1.5$. A possible reason for this may be the presence of extreme disorder in both materials, which prevents the system from building up a long-range correlation and ultimately destroys the critical state. It has been demonstrated that, in

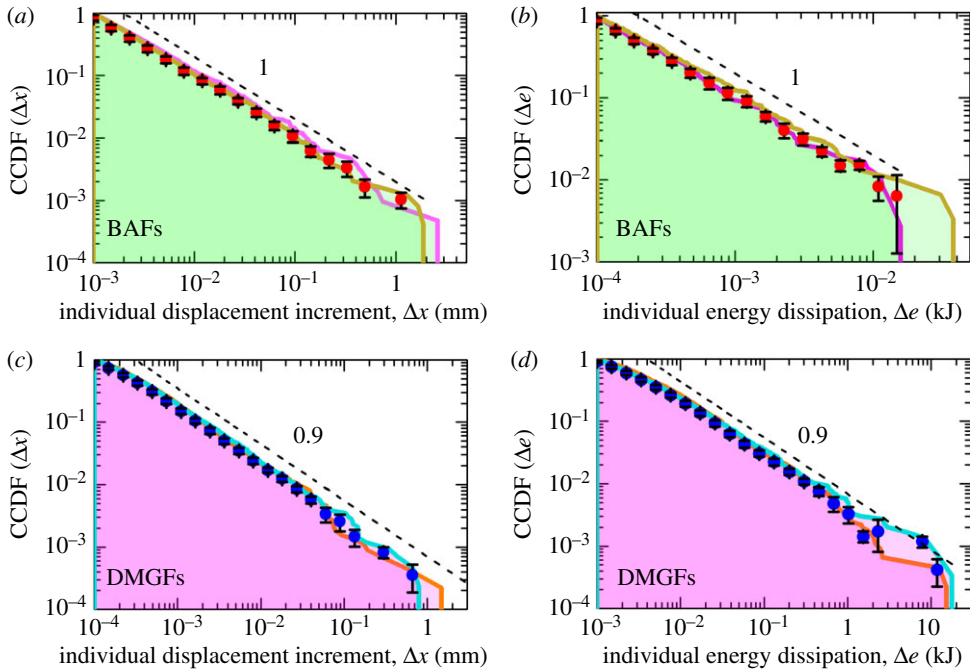


Figure 4. (a,c) The avalanche size distributions based on equation (2.1) that follow a power law, i.e. $\text{CCDF}(\Delta x) \sim \Delta x^{-(\tau_{\Delta x}-1)}$, over several decades of magnitude, suggesting a material-independent exponent $\tau_{\Delta x} = 2$. (b,d) Their corresponding energy dissipation distributions. The solid lines represent different experimental samples, symbols are their average values within a fixed bin size and error bars are the standard deviations. (Online version in colour.)

the presence of randomness or quenched disorder, a system can organize into a stationary state characterized by avalanches with a larger exponent of approximately 2, which is different from the commonly recommended self-organized criticality [51].

(b) Avalanche statistics based on the second definition

To rebuild the long-range correlation destroyed by disorder, we turn to the other avalanche definition, equation (2.2), i.e. the total irreversible displacement that needs to restore the load-carrying capacity of a system from the latest disaster. Figure 5a,c shows the CCDF of S , which exhibits a power-law characteristic, $\text{CCDF}(S) \sim S^{-(\tau_S-1)}$, for both BAFs and DMGFs; their corresponding probability density functions are $P(S) \sim S^{-\tau_S}$. Here, significant deviations in τ_S -values imply that there are two different sorts of universality class in brittle and ductile disordered materials under stress. In the case of BAFs, $P(S)$ is well fitted by using a maximum-likelihood method (see appendix Ac), with $\tau_S = 1.43 \pm 0.05$, which is close to the $\tau_S = 1.5$ predicted by mean-field models [52]. However, a non-trivial scaling exponent, $\tau_S = 1.70 \pm 0.05$, is obtained in DMGFs. That is, extreme events in DMGFs decay faster than those in BAFs. This difference also exists in the distributions of energy dissipation, as shown in figure 5b,d, which reveals a power-law decay with different scaling exponents, $\tau_E = 1.65 \pm 0.03$ in BAFs and $\tau_E = 2.00 \pm 0.05$ in DMGFs. Notably, the discrete bursts based on equation (2.1) tend to follow similar statistics independent of the material type. However, the accumulated sum, defined in equation (2.2), results in the two distinct power-law regimes associated with brittle and ductile samples. This suggests the presence of a relation between the individual bursts with a correlation strength. That is, such a relation is material dependent.

For BAFs, through a simple scaling analysis, we can establish the relationship between τ_S and τ_E as well as other exponents. Here, we have experimentally demonstrated that the avalanche

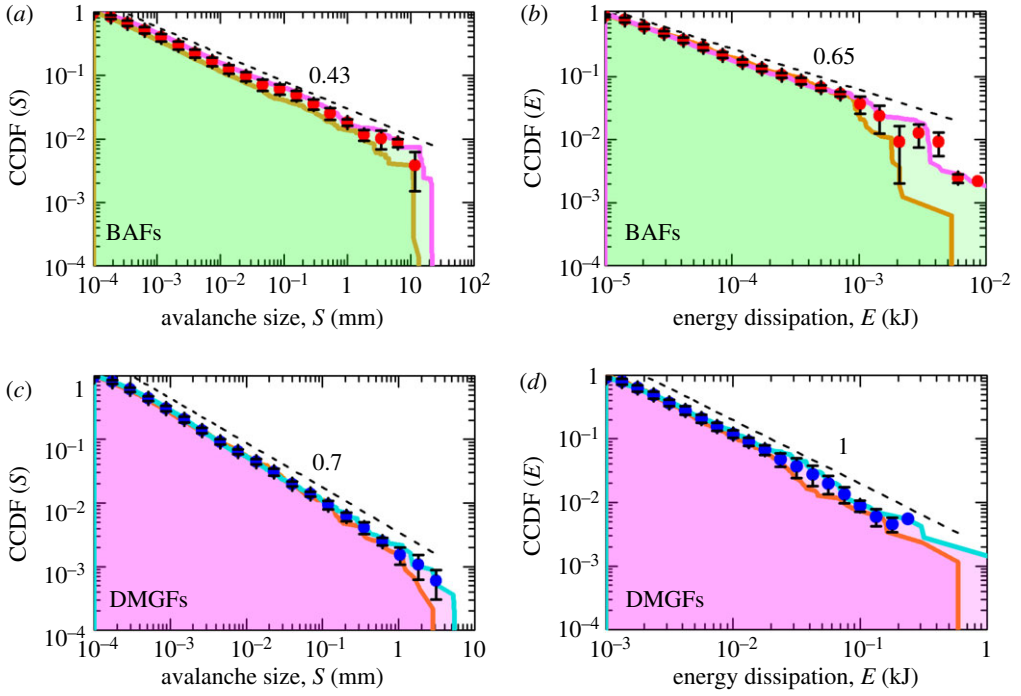


Figure 5. (a,c) The avalanche size distributions based on equation (2.2) that follow a power law, i.e. $\text{CCDF}(S) \sim S^{-(\tau_S-1)}$, over several decades of magnitude, with different τ_S -values for BAFs and DMGFs, respectively. (b,d) Their corresponding energy dissipation distributions. The solid lines represent different experimental samples, symbols are their average values within a fixed bin size and error bars are the standard deviations. (Online version in colour.)

size S satisfies

$$P(S) \sim S^{-\tau_S} G(S/S_m), \quad (3.1)$$

where $G(x)$ is a fast decay function as $x > 1$ and S_m is the cut-off size. Following the notation of Ben-Hur & Biham [53], let us introduce a scaling hypothesis that relates S_m to the characteristic propagation length ξ and time t_m of microcracks, that is,

$$S_m \sim \xi^D, t_m \sim \xi^z, \quad (3.2)$$

where D is the avalanche dimension and z is the dynamical exponent. Based on equations (3.1) and (3.2), we can calculate the average avalanche size, namely

$$\langle S \rangle = \int_0^{S_m} SP(S) dS \sim S_m^{2-\tau_S} \sim \xi^{D(2-\tau_S)}. \quad (3.3)$$

On the other hand, we can calculate $\langle S \rangle$ by using equation (2.2), i.e. $\langle S \rangle \sim N \langle \Delta x \rangle$, where $\langle \Delta x \rangle = \int \Delta x P(\Delta x) d\Delta x \sim \int \Delta x \Delta x^{-2} d\Delta x \sim \ln(\Delta x_c)$. Here, Δx_c is the cut-off of $P(\Delta x)$ and N is the number of subevents in the largest avalanche S_m . Because the accumulated sum, defined in equation (2.2), contains a large number of discrete bursts, the maximum accumulated characteristic length ξ should be larger than Δx_c . Considering the logarithm function is less than a power law, i.e. $\ln(\Delta x_c) < \ln(\xi) < \xi^\alpha$ for $\alpha > 0$, the power-law dependence of $\langle S \rangle$ on ξ can be neglected. That is, the power-law dependence of $\langle S \rangle$ on ξ originates from N . Here, the avalanches in experiments have nothing to do with the specific form of disorder [51], and there is also no other dynamic process involved in BAFs. Thus, the number of subevents Δx per unit time should only depend on the loading rate. In consideration of a constant loading velocity and also a constant triggering

rate of subevents, we have $N \sim t_m \sim \xi^z$. Then,

$$\langle S \rangle \sim N \sim t_m \sim \xi^z. \quad (3.4)$$

Combining equations (3.3) and (3.4), we obtain the first scaling relationship,

$$\tau_S = 2 - \frac{z}{D}. \quad (3.5)$$

In fact, such a scaling relation only applies to the self-organized criticality, where the critical state is stationary, and it does not generally apply to a system that can be tuned to be critical [54].

Analogously, we can calculate the average energy dissipation, $\langle E \rangle = \int EP(E) dE \sim E_m^{2-\tau_E}$, because $E_m = \sigma AS_m$, where σ is the strength and A is the rupture area that scales as ξ^2 , and thus $\langle E \rangle \sim \xi^{(D+2)(2-\tau_E)}$. Moreover, $\langle E \rangle$ can be determined by using equation (2.3), which leads to $\langle E \rangle \sim N \sim \xi^z$. Then, we can have the second scaling relationship,

$$\tau_E = 2 - \frac{z}{D+2}. \quad (3.6)$$

Thus, there are only two independent exponents among (τ_S, τ_E, z, D) , which can be applied to identify a self-organized critical state. The mean-field model predicts the critical exponents, $z = 2$ and $D = 4$ [52], and, based on equations (3.5) and (3.6), we can further calculate $\tau_S = 1.5$ and $\tau_E = 5/3 \approx 1.67$; these values are consistent with experimental observations in BAFs, where $\tau_S = 1.43 \pm 0.05$ and $\tau_E = 1.65 \pm 0.03$.

For DMGFs, we have $\tau_S = 1.70 \pm 0.05$ and $\tau_E = 2.00 \pm 0.05$, which obviously deviate from the scaling relationships (equations (3.5) and (3.6)). These non-trivial exponents are related to plasticity in DMGFs, which can also prevent long-range correlations and ultimately invalidate the scaling hypothesis (equation (3.2)). In fact, a similar avalanche exponent, $\tau_S \approx 1.7$, was recently reported by using a forest fire model, which includes a second kind of tree that is delayed from catching fire to represent the additional process [36]. Our experiments may provide direct experimental evidence that different deformation and collapse mechanisms lead to very different avalanche exponents, which also supports previous experimental studies, such as $\tau_E \simeq 1.7$ (fracture) and $\tau_E \simeq 2$ (twinning-induced plasticity) [55].

In analogy with the relationship $\log_{10} E = 3/2M + 11.8$ in earthquakes, between the released energy E and earthquake magnitude M , and combining with $P(E) dE = P(M) dM$, we have $\tau_E = 1 + 2b/3$, where b is the slope of the Gutenberg–Richter frequency-magnitude relation, i.e. $\log_{10} P(M) = a - bM$ [2]. Thus, we can further estimate the b -value from τ_E , which gives that $b = 0.975 \pm 0.045$ for BAFs and $b = 1.500 \pm 0.075$ for DMGFs. Interestingly, the crossover of b -values from 1 to 1.5 also occurs in scaling of small and large earthquakes [56–58], and our work may provide a new perspective on these natural phenomena.

(c) Distributions of waiting time

For a preselected size S_m , the waiting time is defined as the interval between two successive events with $S > S_m$. The probability density functions, $P(\tau)$, as shown in figure 6a,c for BAFs and DMGFs with different values of S_m , are collapsed onto a single curve by rescaling the vertical and horizontal coordinates with the mean rate of event activities $\langle r \rangle$ or $1/\langle \tau \rangle$ (figure 6b,d). This suggests that there is a generalized scaling formula [4,59], that is,

$$P(\tau) = \langle r \rangle^{\omega/(2-\omega)} F(\tau \langle r \rangle^{1/(2-\omega)}), \quad (3.7)$$

where ω and $F(\cdot)$ are the scaling exponent and function, respectively.

In BAFs, we have $F(x) \sim x^{-\omega}$ with $\omega \approx 1.5$ in the main time range (figure 6b). Thus, equation (3.7) can be reduced to a simple power-law relation, $P(\tau) \sim \tau^{-\omega}$, independent of the mean rate of fracture activities, $\langle r \rangle$. Moreover, a steeper decay emerges on the right tail of the distributions, corresponding to the smaller values of S_m in figure 6a, which leads to a second power-law-like curve as proposed for the system with a non-stationary activity rate [3–5].

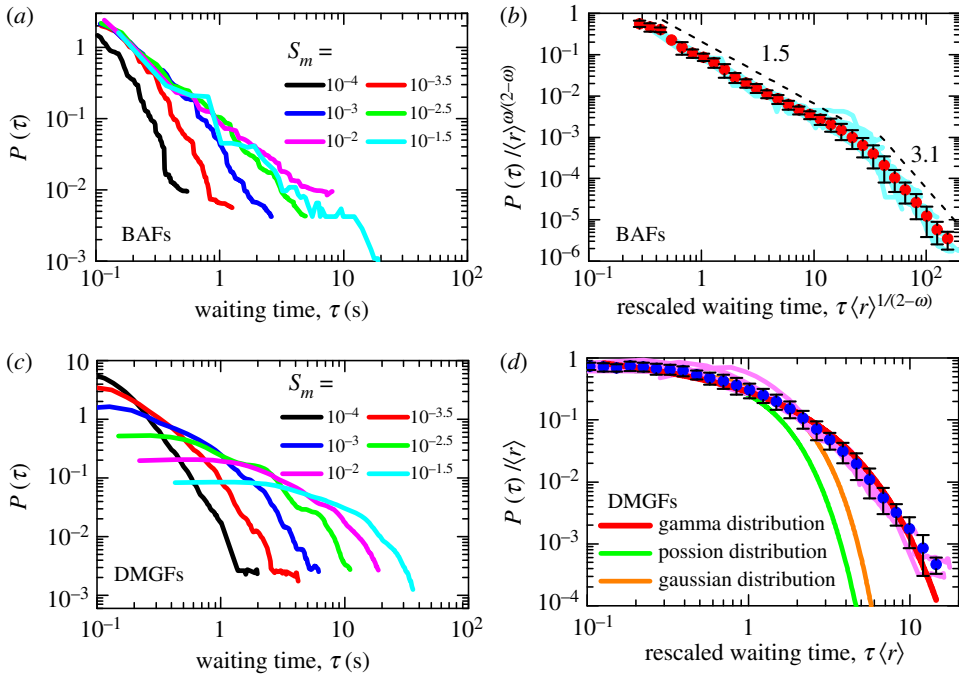


Figure 6. (a,c) The distributions of waiting times with $S > S_m$ for BAFs and DMGFs. (b,d) The waiting times and their distributions rescaled by $\langle r \rangle^{1/(2-\omega)}$ and $\langle r \rangle^{\omega/(2-\omega)}$, where $\langle r \rangle$ is the mean rate of activities. The solid lines represent distributions with different S_m , symbols are their average values within a fixed bin size and error bars are the standard deviations. (Online version in colour.)

A similar crossover was also observed in other brittle porous materials [11–13]. The power-law distributed occurrence time suggests that there is a long temporal correlation [60].

In DMGFs, a distinct scaling behaviour is observed with $\omega \approx 1$. As shown in figure 6d, all distributions are well fitted by a gamma distribution, $F(x) \sim x^{-(1-\gamma)} \exp(-x/a)$ with $\gamma = 0.77 \pm 0.06$ and $a = 1.4 \pm 0.1$. Therefore, we have a decreasing power law with an exponent of approximately 0.23, up to the largest value $x = \tau \langle r \rangle$, where the exponential factor comes into play. The exponential decay suggests the existence of a stationary period, which is related to plastic shear bands. Here, it is worth noting that, in contrast to that in BAFs, such a scaling formula is similar to results (i.e. $\gamma = 0.67 \pm 0.05$ and $a = 1.58 \pm 0.15$) obtained from earthquake catalogues [3–5]. As far as the laboratory scale is concerned, the scaling formula, with almost the same values of γ and a , was also observed in the compression of rocks with a confining pressure [61] and in charcoal dampened with ethanol [62], suggesting universality. Besides the gamma distribution, Poisson and Gaussian distribution functions have also been used to fit experimental data; however, both of them failed to fit the complete dataset well (figure 6d).

(d) Distributions of aftershocks

Next, let us focus on the spatial–temporal correlation of the triggered subsequence. However, before that, we need to define the ‘main shock’ (MS) and ‘aftershock’ (AS) in an avalanche series. Based on the traditional approach, the MS is defined as the events around a narrow selected size band [11–13]; after each MS, the subsequent smaller avalanches consist of an AS sequence. We divide the time from a MS into several parts, and count the number of ASs in each interval to calculate the generation rate. Subsequently, we average the curves over all MSs with size falling into the prescribed interval [13].

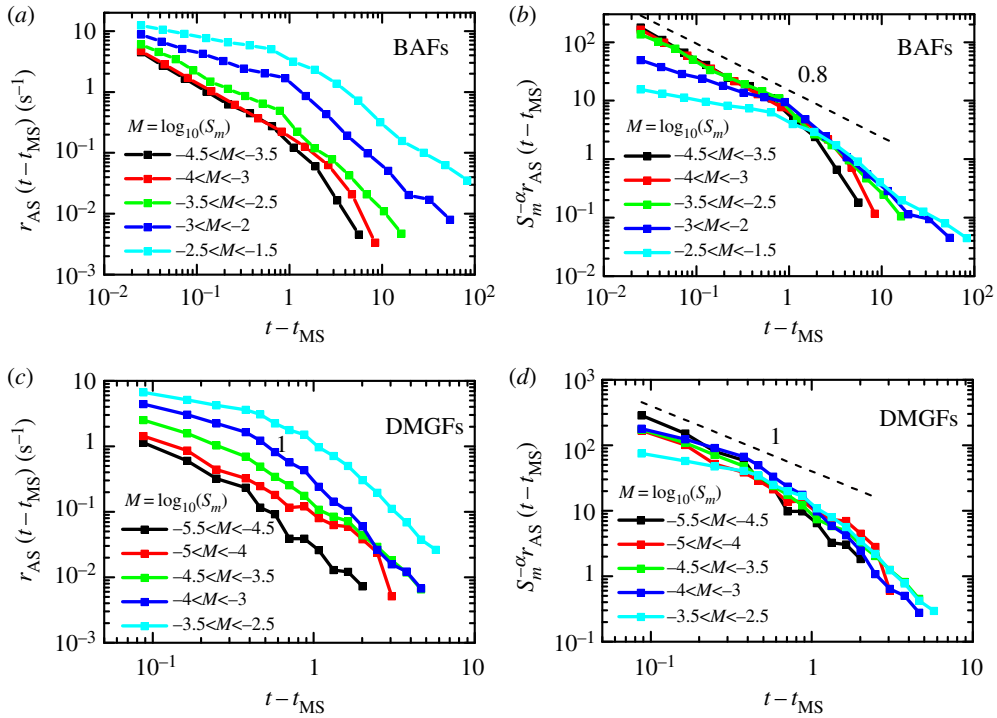


Figure 7. (a,c) The number of aftershocks per unit time, r_{AS} , as a function of time to a main shock, $t - t_{MS}$, for BAFs and DMGFs, respectively, where main shocks are referred to events around a narrow selected size band [11–13]. Dashed lines are power-law functions scaled as $(t - t_{MS})^{-p}$, with different p -values for BAFs and DMGFs. (b,d) Rescaled Omori plots according to the magnitude of triggers. (Online version in colour.)

As seen in figure 7a,c, the time decay of the AS generation rate for these two porous materials exhibits two different regimes: for smaller arguments, it decays as a power law with exponents of approximately 0.8 for BAFs and approximately 1 for DMGFs, corresponding to the p -value in the Omori–Utsu relation [6]; for larger arguments, we find a steeper power-law-like decay for both BAFs and DMGFs. A similar crossover behaviour was also observed in AE experiments [63], which is considered as a lack of spatial information and makes the measurement of the q -value problematic. Furthermore, we show that r_{AS}/S_m^α can be represented as a unified function of $t - t_{MS}$ (figure 7b,d), suggesting $K \sim S_m^\alpha$, which is consistent with the prediction of the productivity law. Interestingly, the exponent α exhibits an obvious insensitivity to material rheological properties ($\alpha \approx 0.4$ for BAFs and $\alpha \approx 0.48$ for DMGFs).

To acquire a more accurate estimation of p -values, and to take advantage of the fact that the larger the event size, the more ASs are triggered, let us extend the definition of MSs to all the events with size larger than S_m . Similarly, we average the curves over all MSs with size falling into the prescribed interval. For each individual AS sequence, the triggering rate follows the modified Omori law, i.e. $r(t) = k/(t_c + t)^p$, where $k \sim S^\alpha$ and p and α are constants independent of the magnitude of the triggers. If we collect sequences with $S > S_m$, and calculate their average value, we have

$$R = \frac{1}{P(S > S_m)} \int_{S_m}^{\infty} P(S) r(t) dS. \quad (3.8)$$

Here, the integral from S_m to infinity is calculated instead of a narrow size band from $S_m - \Delta$ to $S_m + \Delta$. The influence of bin size Δ on AS distributions is shown in figure 8a,b. It can be seen that the increase of Δ can effectively prolong the AS sequence and does not change its distribution. By

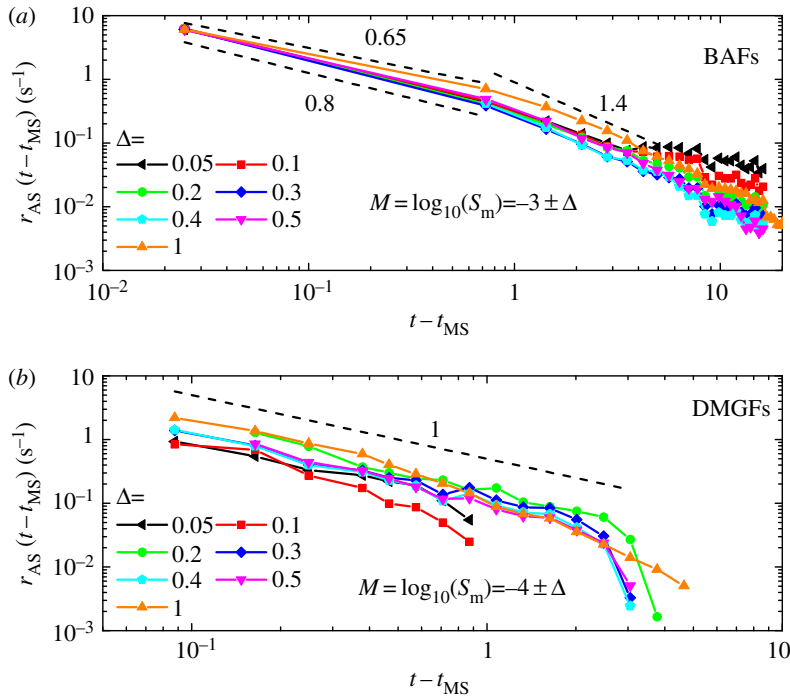


Figure 8. Triggering rate as a function of time averaged over different band sizes Δ . It is seen that the increase of Δ can effectively prolong the aftershock sequence and does not change its distribution. (Online version in colour.)

substituting $P(S) \sim S^{-\tau_S}$ and $P(S > S_m) \sim S_m^{-(\tau_S-1)}$ into equation (3.8), we can further obtain

$$R \sim \frac{1}{S_m^{-\tau_S+1}} \int_{S_m}^{\infty} \frac{S^{-\tau_S+\alpha}}{(t_c+t)^p} dS \sim \frac{S_m^\alpha}{(t_c+t)^p}, \quad (3.9)$$

with the assumption that $\alpha < \tau_S - 1$. Thus, the average AS rate decays with the elapsed time since the MS can preserve the complete information of each AS sequence. That is, this method has an obvious advantage in estimating the p -value, especially for a small value of S_m .

As shown in figure 9a,c, the time decay of AS generation rate for these two porous materials represents a onefold power law, $r_{AS} = K/(t_c + t - t_{MS})^p$, as proposed by Omori [6]. The exponent p is independent of S_m , and, conversely, K and t_c increase with S_m . Similarly, r_{AS}/S_m^α can also be represented as a unified function of $t - t_{MS}$ (figure 9b,d), consistent with the prediction of the productivity law. Interestingly, the exponent α obtained by such an extended definition of MSs (≈ 0.44 for BAFs and ≈ 0.46 for DMGFs) is consistent with the traditional method.

In BAFs, the inherent non-stationarity in brittle fracture leads to a slow decay of AS occurrence rate, which is characterized by a small value, $p = 0.5 \pm 0.1$ (figure 9a). However, in DMGFs, as shown in figure 9c, a faster decay rate of ASs with $p = 0.80 \pm 0.05$ is related to nanoscale shear bands, where plastic energy is dissipated in extremely narrow regions, usually accompanied by thermal softening. The correlation between a higher p -value and heat flow has also been observed in earthquake fault systems [64–66]. Note that, just like other AE experiments of rock fracture, the p -values in both cases are significantly lower than 1, suggesting that the number of ASs is diverging in the long-time limit, i.e. $\int_0^\infty r(t) dt \sim (t + t_c - t_{MS})^{1-p} \rightarrow \infty$, as $p < 1$ and $t \rightarrow \infty$. This can be attributed to the continuous loading process at a short laboratory time scale that leads to an infinite number of triggered events.

Another significant difference in these two porous materials lies in the scaling relationship between t_c and S_m , i.e. $t_c \sim S_m^\eta$, where t_c is the characteristic time; after that, the AS generation rate follows a unified power law, as shown in the insets of figure 9b,d. For BAFs, the observed

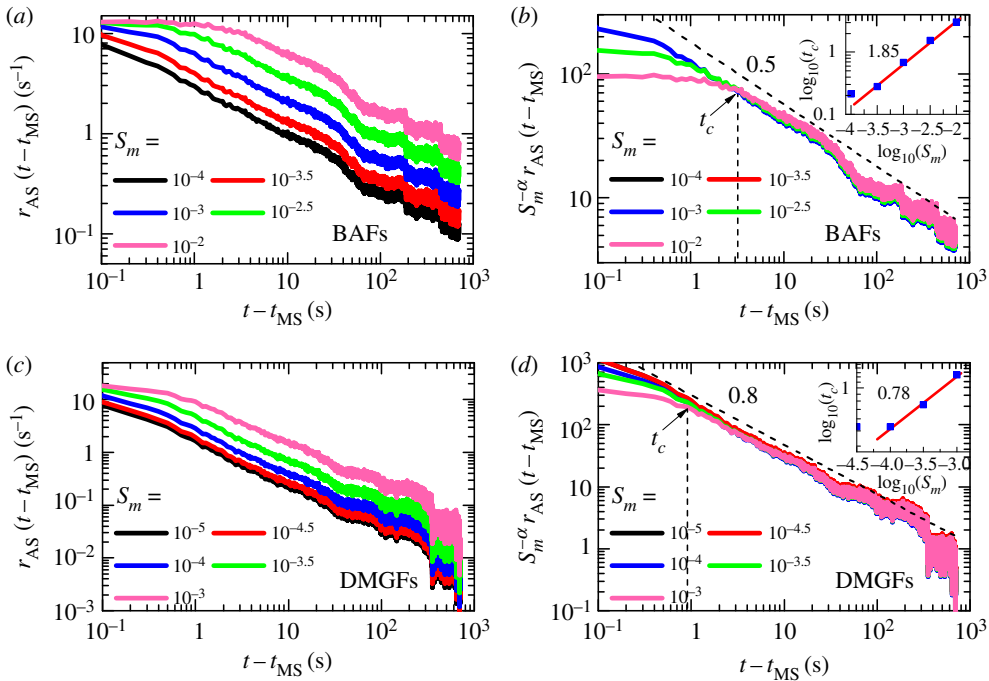


Figure 9. (a,c) The number of aftershocks per unit time, r_{AS} , as a function of time to a main shock, $t - t_{MS}$, for BAFs and DMGFs, respectively, where main shocks are referred to events with $S > S_m$. Dashed lines are power-law functions scaled as $(t - t_{MS})^{-p}$, with different p -values for BAFs and DMGFs. (b,d) Rescaled Omori plots and relations (insets) between the characteristic time t_c and S_m . Here, t_c is the characteristic time, after which the aftershock generation rate follows a power-law decay. (Online version in colour.)

ν value is about 1.85, as shown in the inset of figure 9b, which is much greater than that in DMGFs; see inset of figure 9d. This scaling law allows us to further test the similarity of fractures and avalanches triggered by localized plastic events in laboratory experiments to real earthquakes: for moderate size earthquakes, e.g. 28 September 2004, Mw 6.0 Parkfield, the average slip was measured as approximately 15 cm [67]. Combining the relation $t_c \sim S_m^\nu$ with $\nu \sim 1.85$ and the point ($t_c \sim 1s, S_m \sim 10^{-3}$ mm) from BAFs, we can estimate the characteristic time in earthquakes, $t_c \sim 40\,000$ days. This value is however much greater than that directly calculated from the real earthquake sequence, $t_c \sim 0.13$ days [68]. If we use $\nu = 0.78$ obtained from DMGFs, the characteristic time can be estimated as $t_c \sim 0.126$ days, which is close to the expected one ($t_c \sim 0.13$ days).

(e) The relationship among scaling exponents

Let us consider a time series with N avalanche events. The number of avalanches with size larger than S_m can be calculated by $NP(S > S_m) \sim NS_m^{1-\tau_S}$, which constitutes an MS sequence. Given that MSs are uniformly distributed, the average number of ASs after an MS can be calculated by $\langle N_{AS} \rangle = N[1 - P(S > S_m)]/[NP(S > S_m)]$, that is,

$$\langle N_{AS} \rangle \sim S_m^{\tau_S-1}, \quad (3.10)$$

which can be numerically verified, as shown in figure 10a.

On the other hand, the average number of ASs can be also determined by

$$\langle N_{AS} \rangle = \int_0^{(T_{AS})} r_{AS}(t) dt \sim K(T_{AS})^{1-p}, \quad (3.11)$$

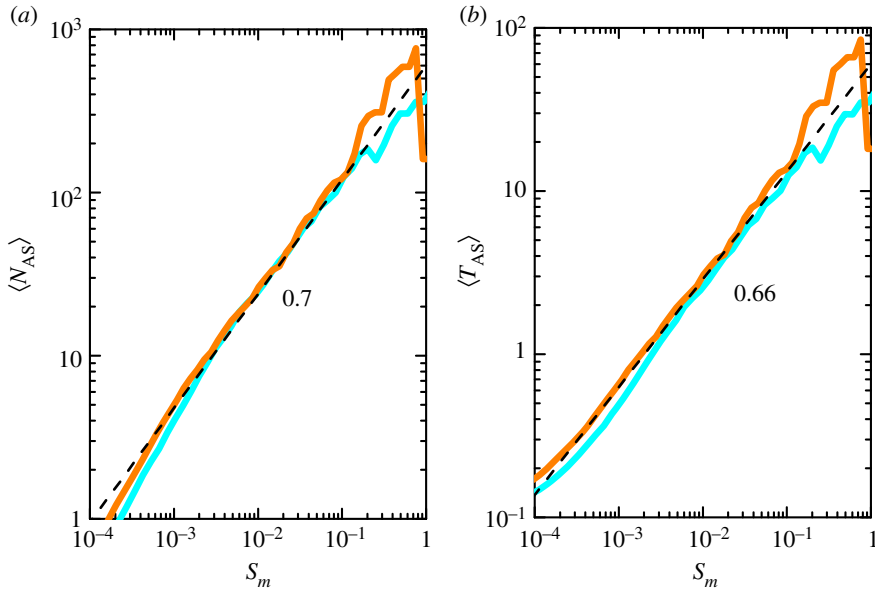


Figure 10. (a) The average number of aftershocks $\langle N_{AS} \rangle$ and (b) the mean waiting time of main shocks $\langle T_{AS} \rangle$ vary with S_m for DMGFs. Both of them follow the scaling of $S_m^{\tau_S-1}$. (Online version in colour.)

where $\langle T_{AS} \rangle$ is the mean duration time of ASs or the mean waiting time of MSs. It scales as the reciprocal of the mean activity rate, i.e. $\langle T_{AS} \rangle \sim 1/\langle r \rangle$, where the mean activity rate $\langle r \rangle$ is related to S_m by $\langle r \rangle \sim S_m^{-(\tau_S-1)}$ [69]. Thus, we can obtain

$$\langle T_{AS} \rangle \sim S_m^{\tau_S-1}, \quad (3.12)$$

which is further verified numerically, as shown in figure 10b.

Combining $K \sim S_m^\alpha$ with equations (3.10), (3.11) and (3.12), we have a scaling relation,

$$\alpha = p(\tau_S - 1). \quad (3.13)$$

As expected, $\tau_S = 1.7$, $p = 0.8$ and $\alpha = 0.46$ in DMGFs are in good agreement with equation (3.13).

In BAFs, however, large-scale events mainly occur at the beginning of a time series, accompanied by the fracture of major support structures. This results in a large number of ASs, at which point the upper limit of the integral in equation (3.11) is independent of S_m . Thus, we obtain another scaling relation,

$$\alpha = \tau_S - 1, \quad (3.14)$$

which compares well with the results of BAFs. The same scaling relation in a form of energy, $\alpha_E = \tau_E - 1$, was reported in AE experiments [70]. Actually, the scaling relation (equation (3.14)) deduced from brittle fracture experiments was found to be valid for earthquakes [70]. For instance, analysis of the seismicity catalogue of Southern California [10] yields $\tau_E = 1.72 \pm 0.07$, $p \approx 0.9$ and $\alpha_E \approx 0.54$, which do not fulfil equation (3.14). Conversely, the newly obtained relationship (equation (3.13)) seems to be well consistent with the outputs of earthquakes.

4. Conclusion

As a new artificial porous material, DMGF with an extremely high strength possesses a stable stress platform under compression. Thus, understanding its deformation mechanism is important

for developing novel energy-absorbing materials. In this paper, we have compared the avalanche dynamics in compression of DMGFs and BAFs, which are dominated by shear banding and fracture, respectively.

To avoid omission in estimating the total released energy, instead of AE signals, we adopted the avalanche size, which is and its corresponding energy dissipation, which can be directly abstracted from the compressed stress time series. Specifically, two definitions of avalanche size were used to characterize the dynamic process of deformation. The first one is the commonly used strain burst, which reflects the transient instability behaviour. Because of the extreme disorder, we obtained a robust scaling exponent, $\tau_{\Delta x, \Delta \epsilon} = 2$ in both materials, which deviates from the self-organized criticality, where $\tau = 1.5$.

To rebuild the long-range correlation destroyed by disorder, we have tried another avalanche size, which is defined as the total irreversible displacement. It is shown that there are two sorts of universality classes, characterized by significantly different power-law exponents. For BAFs, the avalanche size exponent τ_S is approximately 1.5, the energy dissipation exponent τ_E is approximately 1.65 and their corresponding b -value is about 1; these values are consistent with the prediction of self-organized criticality models. In contrast, for DMGFs, a higher avalanche size exponent of 1.7, an energy dissipation exponent of 2 and their corresponding b -value of 1.5 are obtained, suggesting a higher structural stability. This can be attributed to plastic events in DMGFs, which prevent long-range correlations and invalidate the scaling hypothesis at a critical point. The same avalanche exponent τ_S close to 1.7 was also reported by some modified numerical models [36], and the larger $\tau_E \sim 2$ was found in twinning-induced plasticity [55]. These non-trivial scaling behaviours suggest that there is still room for optimization of these material properties, which is different from the most common self-organizing criticality, where no parameters can be tuned.

In addition to avalanche and energy distributions, the statistics of waiting time of these two porous materials are also distinctly different. For BAFs, a power-law distributed waiting time was observed, suggesting a long-time correlation between fracture events; for DMGFs, there was a gamma distribution, implying the existence of an internal characteristic time. Analysis of AS sequences reveals detailed differences in the spatial-temporal correlation of triggered events, characterized by different p -values and scaling relations between t_c and S_m in these two porous materials. Considering the existence of an internal characteristic time in localized plastic dynamics, we further derived a new scaling relationship, which is in good accordance with our experiments. This, in turn, provides good evidence that these non-trivial scaling laws found in DMGFs are connected to an additional plastic process.

Finally, our results allow comments on the viewpoint that compression experiments of disordered materials at the laboratory scale may serve as scaled-down models of earthquake faults. Just from scaling laws, the fracture of brittle porous materials exhibits a striking analogy to small earthquakes, while the shear banding plasticity is more similar to large ones. Thus, our work might also provide a new perspective on such extremal natural phenomena.

Data accessibility. The data that support the findings of this study are available in the electronic supplementary material.

Authors' contributions. H.L. conducted the experiments, analysed the data, sought theoretical interpretation and wrote the paper under the supervision of L.H.D.; all authors participated in the analysis/interpretation of the results, article drafting/editing and critical revisions. All authors approved publication of the final manuscript.

Competing interests. We declare we have no competing interests.

Funding. This work is supported by the National Key Research and Development Program of China (nos. 2017YFB0702003 and 2017YFB0701502), the National Natural Science Foundation of China (nos. 11672316 and 11790292), the Science Challenge Project (no. TZ2016001) and the Opening Fund of State Key Laboratory of Nonlinear Mechanics. C.L. is also grateful for support from the Open Fund of State Key Laboratory for GeoMechanics and Deep Underground Engineering, China University of Mining and Technology (Beijing) (SKLGDUEK1516).

Appendix A

(a) Preparation of ductile metallic glass foams

We chose Vit 1 as a parent material and alumina cenospheres with an average size of 500–600 μm and a relative wall thickness of $t/R = 0.13$ as placeholder particles. DMGFs were fabricated by combination of pressure infiltration invasion and rapid cooling [39].

(b) The spatial resolution of burst displacements

Equation (2.1) allows us to estimate the spatial resolution, i.e. $\delta x \sim \delta F/k$, where k is the stiffness of porous materials. Considering that the stiffness of BAFs and DMGFs is about 9×10^6 and $5 \times 10^7 \text{ Nm}^{-1}$, respectively, and the nominal force uncertainty of a force sensor is of the order of 0.1 N, a displacement increment, Δx_j , less than $\delta F/k \sim 10^{-8} \text{ m}$, is considered as noise. In this paper, we set the cut-off value as 10^{-7} m , above which a power-law distribution is obvious, as shown in figure 5a,c. By using this algorithm, we have an extremely high spatial resolution of approximately 100 nm, which is comparable to an average shear band slip distance (approx. 2 μm) in metallic glasses.

(c) Maximum-likelihood estimation

Suppose that a statistic x follows a power-law distribution, i.e. $P(x) = Ax^{-\tau}$, with a prespecified minimum value, x_{\min} . According to the normalization condition, $\int_{x_{\min}}^{\infty} P(x) dx = 1$, we can obtain

$$A(\tau) = \frac{\tau - 1}{x_{\min}^{-\tau+1}}. \quad (\text{A } 1)$$

Then, the likelihood function for N times of independently and identically distributed tests, (x_1, x_2, \dots, x_N) , can be written as

$$L = \prod_{i=1}^{i=N} P(x_i) = A(\tau)^N \left(\prod_{i=1}^{i=N} x_i \right)^{-\tau}. \quad (\text{A } 2)$$

We can obtain the maximum-likelihood estimate of the parameters τ by maximizing $\ln L$, i.e. solving equation $\partial \ln L / \partial \tau = 0$,

$$\hat{\tau} = 1 + \frac{1}{\frac{1}{N} \sum_{i=1}^N \ln x_i - \ln x_{\min}}, \quad (\text{A } 3)$$

where the value of x_{\min} can be determined by the cut-off Δx (see appendix Ab).

References

1. Wadati K. 1932 On the frequency distribution of earthquakes. *J. Meteorol. Soc. Jpn. Ser. II* **10**, 559–568. (doi:10.2151/jmsj1923.10.10_559)
2. Gutenberg B, Richter CF. 1956 Earthquake magnitude, intensity, energy, and acceleration. *Bull. Seismol. Soc. Am.* **46**, 105.
3. Corral A. 2003 Local distributions and rate fluctuations in a unified scaling law for earthquakes. *Phys. Rev. E* **68**, 035102. (doi:10.1103/PhysRevE.68.035102)
4. Corral Á. 2004 Long-term clustering, scaling, and universality in the temporal occurrence of earthquakes. *Phys. Rev. Lett.* **92**, 108501. (doi:10.1103/PhysRevLett.92.108501)
5. Corral Á. 2004 Universal local versus unified global scaling laws in the statistics of seismicity. *Physica A* **340**, 590. (doi:10.1016/j.physa.2004.05.010)
6. Omori F. 1894 On the after-shocks of earthquakes. *J. College Sci., Imperial University, Tokyo* **7**, 111.
7. Utsu T, Ogata Y, Ritsuko S, Matsuúra S. 1995 The centenary of the Omori formula for a decay law of aftershock activity. *J. Phys. Earth* **43**, 1. (doi:10.4294/jpe1952.43.1)

8. Shcherbakov R, Turcotte DL, Rundle JB. 2004 A generalized Omori's law for earthquake aftershock decay. *Geophys. Res. Lett.* **31**, L11613. (doi:10.1029/2004GL019808)
9. Sornette D, Ouillon G. 2005 Multifractal scaling of thermally activated rupture processes. *Phys. Rev. Lett.* **94**, 038501. (doi:10.1103/PhysRevLett.94.038501)
10. Helmstetter A. 2003 Is earthquake triggering driven by small earthquakes. *Phys. Rev. Lett.* **91**, 058501. (doi:10.1103/PhysRevLett.91.058501)
11. Baró J, Planes A, Salje EK, Schranz W, Soto-Parra DE, Vives E. 2013 Statistical similarity between the compression of a porous material and earthquakes. *Phys. Rev. Lett.* **110**, 088702. (doi:10.1103/PhysRevLett.110.088702)
12. Nataf GF, Castillo-Villa PO, Baró J, Illa X, Vives E, Planes A, Salje EK. 2014 Avalanches in compressed porous SiO₂-based materials. *Phys. Rev. E* **90**, 022405. (doi:10.1103/PhysRevE.90.022405)
13. Mäkinen T, Miksic A, Ovaska M, Alava MJ. 2015 Avalanches in wood compression. *Phys. Rev. Lett.* **115**, 055501. (doi:10.1103/PhysRevLett.115.055501)
14. Tsai ST, Wang LM, Huang P, Yang Z, Chang CD, Hong TM. 2016 Acoustic emission from breaking a bamboo chopstick. *Phys. Rev. Lett.* **116**, 035501. (doi:10.1103/PhysRevLett.116.035501)
15. Flyvbjerg H, Sneppen K, Bak P. 1993 Mean field theory for a simple model of evolution. *Phys. Rev. Lett.* **71**, 4087. (doi:10.1103/PhysRevLett.71.4087)
16. Zapperi S, Lauritsen KB, Stanley HE. 1995 Self-organized branching processes: mean-field theory for avalanches. *Phys. Rev. Lett.* **75**, 4071. (doi:10.1103/PhysRevLett.75.4071)
17. Alava MJ, Nukala PK, Zapperi S. 2006 Statistical models of fracture. *Adv. Phys.* **55**, 349. (doi:10.1080/00018730300741518)
18. Dahmen KA, Ben-Zion Y, Uhl JT. 2009 Micromechanical model for deformation in solids with universal predictions for stress-strain curves and slip avalanches. *Phys. Rev. Lett.* **102**, 175501. (doi:10.1103/PhysRevLett.102.175501)
19. Fondriest M, Smith SA, Di Toro G, Zampieri D, Mitterpergher S. 2012 Fault zone structure and seismic slip localization in dolostones, an example from the Southern Alps, Italy. *J. Struct. Geol.* **45**, 52. (doi:10.1016/j.jsg.2012.06.014)
20. Platt JD, Rudnicki JW, Rice JR. 2014 Stability and localization of rapid shear in fluid-saturated fault gouge: 2. Localized zone width and strength evolution. *J. Geophys. Res.: Solid Earth* **119**, 4334. (doi:10.1002/2013JB010711)
21. Rice JR, Rudnicki JW, Platt JD. 2014 Stability and localization of rapid shear in fluid-saturated fault gouge: 1. Linearized stability analysis. *J. Geophys. Res.: Solid Earth* **119**, 4311. (doi:10.1002/2013JB010710)
22. Falk ML, Langer JS. 2011 Deformation and failure of amorphous, solidlike materials. *Annu. Rev. Condens. Matter Phys.* **2**, 353. (doi:10.1146/annurev-conmatphys-062910-140452)
23. Palmer AC, Rice JR. 1973 The growth of slip surfaces in the progressive failure of over-consolidated clay. *Proc. R. Soc. A* **332**, 527–548. (doi:10.1098/rspa.1973.0040)
24. Puzrin AM, Germanovich L. 2005 The growth of shear bands in the catastrophic failure of soils. *Proc. R. Soc. A* **461**, 1199–1228. (doi:10.1098/rspa.2004.1378)
25. Germanovich LN, Kim S, Puzrin AM. 2016 Dynamic growth of slip surfaces in catastrophic landslides. *Proc. R. Soc. A* **472**, 20150758. (doi:10.1098/rspa.2015.0758)
26. Spaepen F. 1977 A microscopic mechanism for steady state inhomogeneous flow in metallic glasses. *Acta Metall.* **25**, 407. (doi:10.1016/0001-6160(77)90232-2)
27. Argon A. 1979 Plastic deformation in metallic glasses. *Acta Metall.* **27**, 47. (doi:10.1016/0001-6160(79)90055-5)
28. Sun B, Yu H, Jiao W, Bai H, Zhao D, Wang W. 2010 Plasticity of ductile metallic glasses: a self-organized critical state. *Phys. Rev. Lett.* **105**, 035501. (doi:10.1103/PhysRevLett.105.035501)
29. Antonaglia J, Wright WJ, Gu X, Byer RR, Hufnagel TC, LeBlanc M, Uhl JT, Dahmen KA. 2014 Bulk metallic glasses deform via slip avalanches. *Phys. Rev. Lett.* **112**, 155501. (doi:10.1103/PhysRevLett.112.155501)
30. Baró J, Davidsen J. 2018 Universal avalanche statistics and triggering close to failure in a mean-field model of rheological fracture. *Phys. Rev. E* **97**, 033002. (doi:10.1103/PhysRevE.97.033002)
31. Baró J, Dahmen KA, Davidsen J, Planes A, Castillo PO, Nataf GF, Salje EK, Vives E. 2018 Experimental evidence of accelerated seismic release without critical failure in acoustic emissions of compressed nanoporous materials. *Phys. Rev. Lett.* **120**, 245501. (doi:10.1103/PhysRevLett.120.245501)

32. Lyakhovsky V, Ben-Zion Y, Agnon A. 2005 A viscoelastic damage rheology and rate-and state-dependent friction. *Geophys. J. Int.* **161**, 179. (doi:10.1111/j.1365-246X.2005.02583.x)
33. Lyakhovsky V, Hamiel Y, Ben-Zion Y. 2011 A non-local visco-elastic damage model and dynamic fracturing. *J. Mech. Phys. Solids* **59**, 1752. (doi:10.1016/j.jmps.2011.05.016)
34. Ruina A. 1983 Slip instability and state variable friction laws. *J. Geophys. Res.: Solid Earth* **88**, 10359. (doi:10.1029/JB088iB12p10359)
35. Jagla E, Kolton A. 2010 A mechanism for spatial and temporal earthquake clustering. *J. Geophys. Res.* **115**, B05312. (doi:10.1029/2009JB006974)
36. Jagla EA. 2013 Forest-fire analogy to explain the b value of the Gutenberg-Richter law for earthquakes. *Phys. Rev. Lett.* **111**, 238501. (doi:10.1103/PhysRevLett.111.238501)
37. Jagla EA, Landes FP, Rosso A. 2014 Viscoelastic effects in avalanche dynamics: a key to earthquake statistics. *Phys. Rev. Lett.* **112**, 174301. (doi:10.1103/PhysRevLett.112.174301)
38. Demetriou MD, Veazey C, Harmon JS, Schramm JP, Johnson WL. 2008 Stochastic metallic-glass cellular structures exhibiting benchmark strength. *Phys. Rev. Lett.* **101**, 145702. (doi:10.1103/PhysRevLett.101.145702)
39. Lin H, Wang H, Lu C, Dai L. 2016 A metallic glass syntactic foam with enhanced energy absorption performance. *Scr. Mater.* **119**, 47. (doi:10.1016/j.scriptamat.2016.03.034)
40. Vasseur J, Wadsworth FB, Lavalley Y, Bell AF, Main IG, Dingwell DB. 2015 Heterogeneity: the key to failure forecasting. *Sci. Rep.* **5**, 13259. (doi:10.1038/srep13259)
41. Pérez-Reche FJ, Truskinovsky L, Zanzotto G. 2008 Driving-induced crossover: from classical criticality to self-organized criticality. *Phys. Rev. Lett.* **101**, 230601. (doi:10.1103/PhysRevLett.101.230601)
42. Maaß R, Wraith M, Uhl J, Greer J, Dahmen K. 2015 Slip statistics of dislocation avalanches under different loading modes. *Phys. Rev. E* **91**, 042403. (doi:10.1103/PhysRevE.91.042403)
43. Larson KM, Freymueller JT, Philipsen S. 1997 Global plate velocities from the Global Positioning System. *J. Geophys. Res.: Solid Earth* **102**, 9961. (doi:10.1029/97JB00514)
44. Scholz C. 1968 Microfracturing and the inelastic deformation of rock in compression. *J. Geophys. Res.* **73**, 1417. (doi:10.1029/JB073i004p01417)
45. Hirata T. 1987 Omori's power law aftershock sequences of microfracturing in rock fracture experiment. *J. Geophys. Res.: Solid Earth* **92**, 6215. (doi:10.1029/JB092iB07p06215)
46. Roux S, Guyon E. 1989 Temporal development of invasion percolation. *J. Phys. A: Math. Gen.* **22**, 3693. (doi:10.1088/0305-4470/22/17/034)
47. Tanguy A, Gounelle M, Roux S. 1998 From individual to collective pinning: effect of long-range elastic interactions. *Phys. Rev. E* **58**, 1577. (doi:10.1103/PhysRevE.58.1577)
48. Talamali M, Petäjä V, Vandembroucq D, Roux S. 2011 Avalanches, precursors, and finite-size fluctuations in a mesoscopic model of amorphous plasticity. *Phys. Rev. E* **84**, 016115. (doi:10.1103/PhysRevE.84.016115)
49. Barés J, Hattali M, Dalmas D, Bonamy D. 2014 Fluctuations of global energy release and crackling in nominally brittle heterogeneous fracture. *Phys. Rev. Lett.* **113**, 264301. (doi:10.1103/PhysRevLett.113.264301)
50. Chen H, He Y, Shiflet G, Poon S. 1994 Deformation-induced nanocrystal formation in shear bands of amorphous alloys. *Nature* **367**, 541–543. (doi:10.1038/367541a0)
51. Newman M, Sneppen K. 1996 Avalanches, scaling, and coherent noise. *Phys. Rev. E* **54**, 6226. (doi:10.1103/PhysRevE.54.6226)
52. Vespignani A, Zapperi S. 1998 How self-organized criticality works: a unified mean-field picture. *Phys. Rev. E* **57**, 6345. (doi:10.1103/PhysRevE.57.6345)
53. Ben-Hur A, Biham O. 1996 Universality in sandpile models. *Phys. Rev. E* **53**, R1317. (doi:10.1103/PhysRevE.53.R1317)
54. Paczuski M, Maslov S, Bak P. 1996 Avalanche dynamics in evolution, growth, and depinning models. *Phys. Rev. E* **53**, 414. (doi:10.1103/PhysRevE.53.414)
55. Soto-Parra D, Zhang X, Cao S, Vives E, Salje EK, Planes A. 2015 Avalanches in compressed Ti-Ni shape-memory porous alloys: an acoustic emission study. *Phys. Rev. E* **91**, 060401. (doi:10.1103/PhysRevE.91.060401)
56. Romanowicz B, Rundle JB. 1993 On scaling relations for large earthquakes. *Bull. Seismol. Soc. Am.* **83**, 1294.
57. Rundle JB. 1989 Derivation of the complete Gutenberg-Richter magnitude-frequency relation using the principle of scale invariance. *J. Geophys. Res.: Solid Earth* **94**, 12337. (doi:10.1029/JB094iB09p12337)

58. Pacheco JF, Scholz CH, Sykes LR. 1992 Changes in frequency–size relationship from small to large earthquakes. *Nature* **355**, 71. (doi:10.1038/355071a0)
59. Bak P, Christensen K, Danon L, Scanlon T. 2002 Unified scaling law for earthquakes. *Phys. Rev. Lett.* **88**, 178501. (doi:10.1103/PhysRevLett.88.178501)
60. Shcherbakov R, Yakovlev G, Turcotte DL, Rundle JB. 2005 Model for the distribution of aftershock interoccurrence times. *Phys. Rev. Lett.* **95**, 218501. (doi:10.1103/PhysRevLett.95.218501)
61. Davidsen J, Stanchits S, Dresen G. 2007 Scaling and universality in rock fracture. *Phys. Rev. Lett.* **98**, 125502. (doi:10.1103/PhysRevLett.98.125502)
62. Ribeiro H, Costa L, Alves L, Santoro P, Picoli S, Lenzi E, Mendes R. 2015 Analogies between the cracking noise of ethanol-dampened charcoal and earthquakes. *Phys. Rev. Lett.* **115**, 025503. (doi:10.1103/PhysRevLett.115.025503)
63. Davidsen J, Kwiatak G, Charalampidou EM, Goebel T, Stanchits S, Rück M, Dresen G. 2017 Triggering processes in rock fracture. *Phys. Rev. Lett.* **119**, 068501. (doi:10.1103/PhysRevLett.119.068501)
64. Kisslinger C, Jones LM. 1991 Properties of aftershock sequences in southern California. *J. Geophys. Res.: Solid Earth* **96**, 11947. (doi:10.1029/91JB01200)
65. Bohnenstiehl D, Tolstoy M, Dziak R, Fox C, Smith D. 2002 Aftershock sequences in the mid-ocean ridge environment: an analysis using hydroacoustic data. *Tectonophysics* **354**, 49. (doi:10.1016/S0040-1951(02)00289-5)
66. Rabinowitz N, Steinberg DM. 1998 Aftershock decay of three recent strong earthquakes in the Levant. *Bull. Seismol. Soc. Am.* **88**, 1580.
67. Langbein J. 2005 Preliminary report on the 28 September 2004, M 6.0 Parkfield, California earthquake. *Seismol. Res. Lett.* **76**, 10. (doi:10.1785/gssrl.76.1.10)
68. Shcherbakov R, Turcotte DL, Rundle JB. 2006 Scaling properties of the Parkfield aftershock sequence. *Bull. Seismol. Soc. Am.* **96**, S376. (doi:10.1785/0120050815)
69. Corral A. 2006 Dependence of earthquake recurrence times and independence of magnitudes on seismicity history. *Tectonophysics* **424**, 177. (doi:10.1016/j.tecto.2006.03.035)
70. Barés J, Dubois A, Hattali L, Dalmas D, Bonamy D. 2018 Aftershock sequences and seismic-like organization of acoustic events produced by a single propagating crack. *Nat. Commun.* **9**, 1253. (doi:10.1038/s41467-018-03559-4)